Supplement of Atmos. Chem. Phys., 25, 12007–12035, 2025
https://doi.org/10.5194/acp-25-12007-2025-supplement

Atmospheric Chemistry and Physics
Open Access
EGU

Supplement of

Locally emitted fungal spores serve as high-temperature ice nucleating particles in the European sub-Arctic

Jürgen Gratzl et al.

Correspondence to: Hinrich Grothe (hinrich.grothe@tuwien.ac.at)

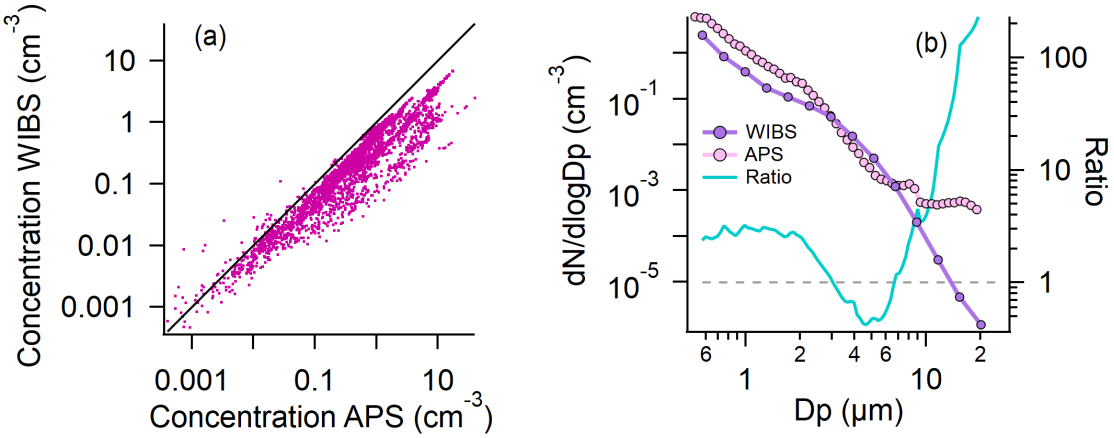

Figure S1. (a) Scatter plot of TAP concentrations measured with WIBS vs. concentrations of particles with aerodynamic diameter > 523 nm measured with APS with 30 min resolution. The black line represents the 1:1 line. (b) comparison of arithmetic mean size distributions during the PaCE22 campaign of TAPs of WIBS and APS and their ratio.

S1 Comparison of WIBS and APS

An Aerodynamic Particle Sizer (TSI, USA) APS was operated alongside WIBS to compare particle concentrations and validate WIBS data. The APS measures particles with an aerodynamic diameter >0.523 nm. 30 min mean values of APS data and total aerosol particles (TAPs) from WIBS were calculated and compared during the PaCE22 campaign. APS concentrations were on average 3 times higher than those recorded by WIBS. A scatter plot can be seen in Fig. S1 (a). Average size distributions of TAPs measured by both the WIBS and APS during the entire PaCE22 campaign are shown in Fig. S1 (b). It needs to be noted that both devices use different approaches for size-classification (optical versus aerodynamic) and are hence not directly comparable. On average, WIBS recorded higher concentrations for particles in the 3–7 $\mu\mathrm{m}$ size range, whereas concentrations for particles smaller than 3 $\mu\mathrm{m}$ and larger than 7 $\mu\mathrm{m}$ were lower than those measured by the APS. The lower concentrations of larger particles detected by WIBS are likely due to particle losses in its inlet system (Gratzl et al., 2025). Additionally, because the aerodynamic diameter (measured by APS) tends to be larger than the optical equivalent diameter (measured by WIBS), APS may have registered smaller particles as belonging to larger size bins, contributing to higher concentrations at smaller sizes compared to WIBS.

S2 A closer look on the other HFAP types

Figure S2, presents daily mean concentrations of TAPs, highly fluorescent aerosol particles (HFAPs) and all types of HFAPs, alongside temperature and snow depth, both measured at Kenttärova research station (N67°59.237', E24°14.579) inside the forest near Sammaltunturi. Seasons were defined based on daily mean temperatures: autumn (< 10 °C), winter (mostly < 0 °C),

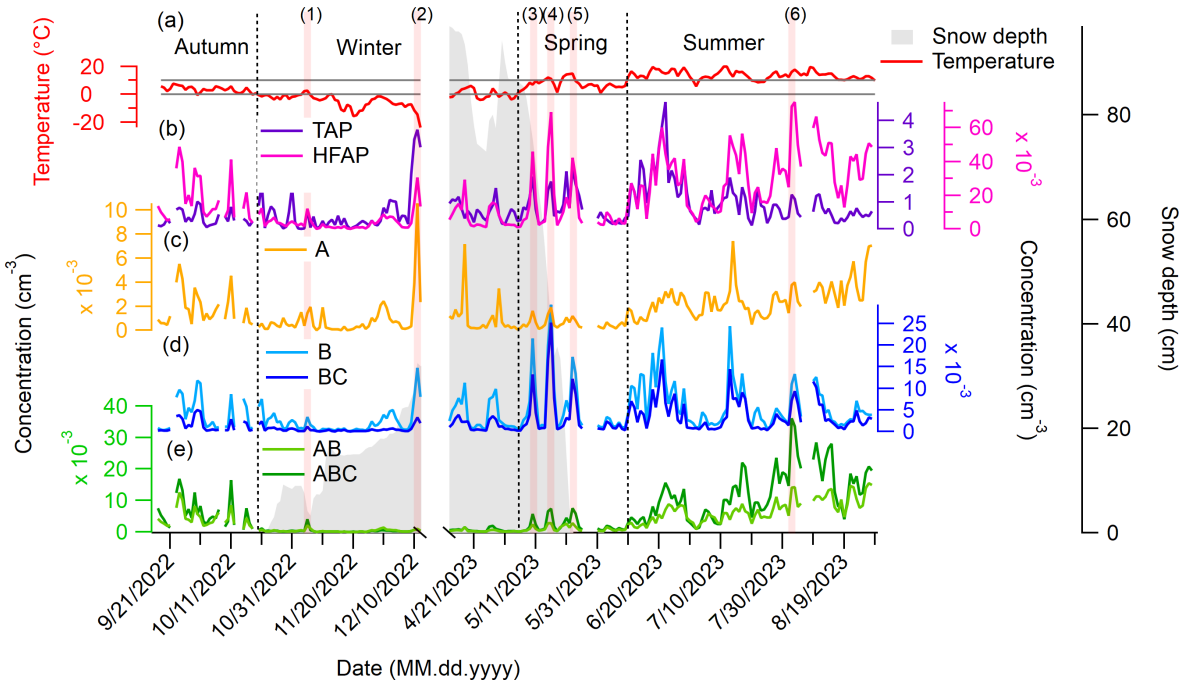

Figure S2. Daily mean concentrations of TAPs, HFAPs und all fluorescent particle types, mean snow depth and ambient temperature inside a near spruce forest. (a) Temperature measured at Kenttärova station is used to define the meteorological seasons. (b) TAPS and HFAPs, (c) A particles, (d) B and BC particles, (e) AB and ABC particles. Horizontal transparent red lines are labeled with a number and mark certain days discussed in the text.

spring (mostly between 0 °C and 10 °C) and summer (mostly over 10 °C). Winter started three days before permanent snow cover and ended 3 days after snow melt began. The polar night started on December 21. Spring included most of the snow melt period and extended 17 days into the snow-free period. Median values, 25th and 75th percentiles and fractions of TAPs and all HFAP types together with meteorological parameter for the four seasons are summarized in Tab. S1.

A seasonal trend is apparent for A particles (Fig. S2 (c)), with the highest median concentration in summer (2.2×10^{-3} cm^{-3}). However, notable peaks also occured in winter. Figure S4 (e) shows, that many daily mean size distributions during the snow covered period showed higher concentrations for particles < 1 µm than during the snow free period, while larger particles dominated during warmer periods. For instance, the day of maximum concentration coincided with the maximum of TAPs during winter, on December 11th (labeled (2) in Fig. S2 (a)). On this day, air masses originated from Western Russia, suggesting long-range transport. Size distributions indicate that both A particles and HFAPs were smaller compared to peak days in other seasons. As the arriving air masses went over industrialized areas, this suggests a possible anthropogenic origin. A more detailed description of this event can be read in sect. S3.2. Summer diurnal trends (Fig. S3) show that A particles and ambient temperature both underwent a very similar trend over the day. In chamber experiments, bacteria have been classified almost exclusively as A particles (Savage et al., 2017; Hernandez et al., 2016), although only a single field study confirmed

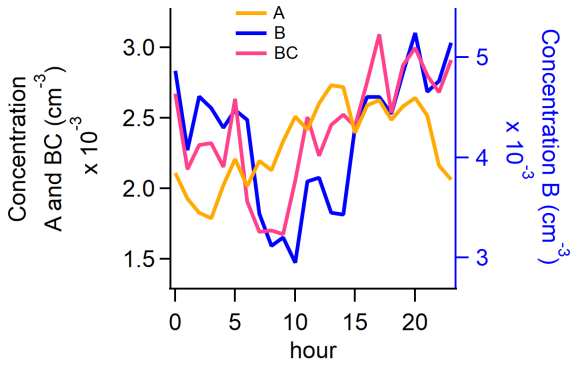

Figure S3. Diurnal cycle of summertime concentrations of A, B and BC particles. Diurnal trends of in-cloud frequency, ambient temperature, TAPs and other HFAP types are depicted in the main manuscript in Fig. 4.

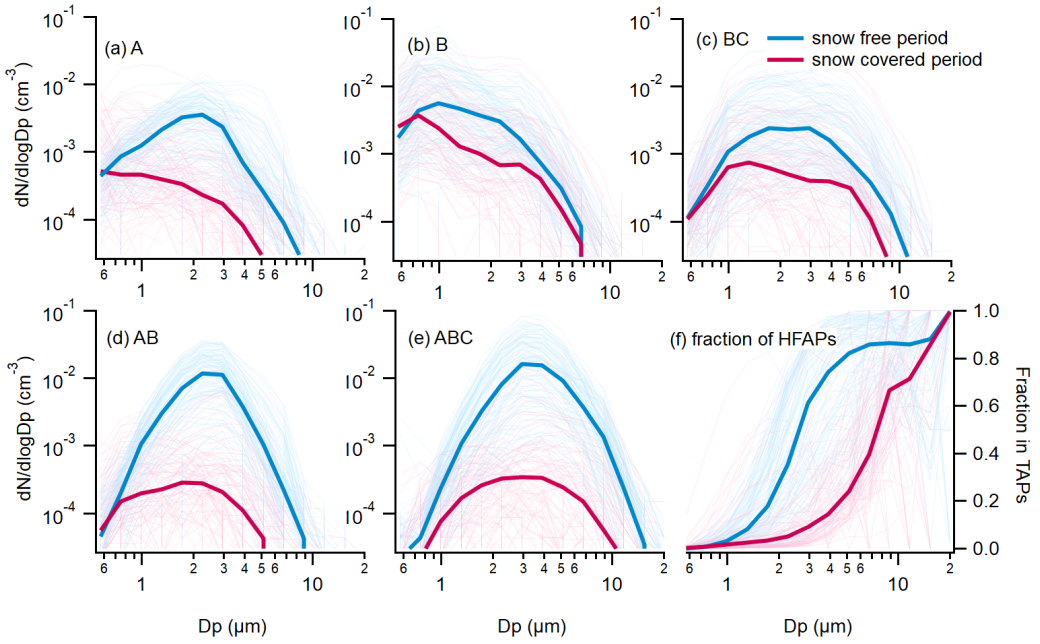

Figure S4. (a)-(g): Size distributions of all particles types measured with WIBS. (h) Fraction of HFAPs per particles size. Thick blue lines: Median distributions during snow free periods. Soft blue lines: Daily mean distributions during snow free periods. Thick red lines: Median distributions during snow covered period. Soft red lines: Daily mean distributions during snow covered period.

this correlation (Katsivela et al., 2025). Previous research (Lighthart and Shaffer, 1995; Abdel Hameed et al., 2009) observed afternoon accumulation peaks for airborne bacteria, indicating a possible connection between ambient temperature and the emission of bacteria. Diesel soot, also tested by Savage et al. (2017), fluoresces in the A channel as well, implying that A particles here likely included both anthropogenic aerosols and bacteria, with anthropogenic influence being stronger in winter.

The concentration of bacteria over vegetated surfaces (close to forested ground and high alpine) was estimated to be $\approx 10^4$ m^{-3} (Healy et al., 2014; Bauer et al., 2002; Burrows et al., 2009; Després et al., 2012). This is one order of magnitude greater than the concentration of A particles measured here.

B and BC particles (Fig. S2 (d)) showed similar behavior, both correlating strongly with TAPs (Pearson r = 0.66 for B particles and 0.52 for BC particles, $\mathrm{p} < 0.0001$). While BC particles lacked a clear seasonal cycle, their concentration appears suppressed by snow cover from October to December 2022, resulting in the lowest median levels in winter (3.6×10^{-4} cm^{-3}). The highest concentration of BC particles was in summer with 2.3×10^{-3} cm^{-3}. The median concentration of B particles was the most consistent over the seasons with lowest in winter (1.3×10^{-4} cm^{-3}) and highest in summer (4.0×10^{-3} cm^{-3}). From April 2023 onward, BC concentration trends closely followed B particles, with three prominent springtime peaks (labeled (3), (4), and (5) in Fig. S2 (a)). On days (4) and (5), air masses spend most of the prior three days over the gulf of Bothnia, or its eastern coastline, suggesting a possible coastal inversion, from where enriched anthropogenic aerosol could have been transported to Pallas. These peaks also aligned with elevated eBC concentrations. A detailed description of these events can be seen in sect. S3.3. B and BC particles, although likely heavily influenced by anthropogenic sources due to their high correlation with eBC mass concentration (see Sect. 3.4 in the main text), followed the summertime diurnal trend of all HFAPs (Fig.S3), suggesting local anthropogenic emissions, rather than far range transported ones were important for this signal. Biomass burning from local or regional population and vehicle exhaustion may contribute to their presence.

S3 Case studies

S3.1 November 5, 2022: Temporary snow melt

Permanent snow cover significantly reduced HFAP concentrations, particularly AB and ABC particles. On November 5, 2022, a brief melting period coincided with a sharp increase in AB and ABC particles. To determine whether this rise was caused by snow melt or a shift in air mass direction, we calculated 72 h back trajectories for this day as well as the day before and after (Fig.S5 (a)). Since no major change in air mass direction occurred, local meteorological conditions were likely responsible. In Fig.S5 (b), size distributions of ABC particles show a strong increase in ≈ 3 $\mu\mathrm{m}$ particles around 6 am UTC on November 5. Snow depth (measured at 6 am UTC) in Pallas, indicates that melting began two days earlier. In Kolari only 70 km south of Pallas, snow has completely melted by 6 am UTC on November 5. This suggests that biological activity increased immediately after snow melt, with air masses transporting biological particles from the snow-free biosphere south of Pallas.

S3.2 December 11, 2022: Peak A concentration

On December 11, 2022, the highest A concentrations and elevated TAP levels were recorded. On this day, air masses primarily arrived from Western Russia (Fig. S6 (a)), passing over the Central Economic Region, a highly industrialized area. Figure S6

Table S1. Median concentration values and percentiles (25th and 75th) of TAPs, HFAPs and particles types for every season and meteorological parameters. All concentration values are reported in $\mathrm{std\,cm^{-3}}$.

Season	Autumn	Winter	Spring	Summer
Dates	Sept 17 2022- Oct 17 2022	Oct 18 2022- Dec 12 2022, April 13 2023- May 5 2023	May 5 2023- June 9 2023	June 10 2023- Aug 28 2023
hours of data	287	1727	658	1743
Median TAP	2.8×10^{-1}	3.3×10^{-1}	4.4×10^{-1}	7.5×10^{-1}
Percentiles TAP	1.2×10^{-1};6.2×10^{-1}	8.2×10^{-2};8.8×10^{-1}	2.5×10^{-1};1.2	4.5×10^{-1};1.4
Median HFAP	1.2×10^{-2}	2.9×10^{-3}	5.4×10^{-3}	3.0×10^{-2}
Percentiles HFAP	5.81×10^{-3};2.83×10^{-2}	1.2×10^{-3};6.8×10^{-3}	2.9×10^{-3};1.4×10^{-2}	1.5×10^{-2};4.5×10^{-2}
Median fraction HFAP	5.6×10^{-2}	1.0×10^{-2}	1.4×10^{-2}	3.5×10^{-2}
Percentiles of fraction	3.4×10^{-2};8.8×10^{-2}	4.9×10^{-3};2.0×10^{-2}	6.7×10^{-3};2.6×10^{-2}	1.7×10^{-2};7.0×10^{-2}
Median A	1.2×10^{-3}	3.7×10^{-4}	3.7×10^{-4}	2.2×10^{-3}
Percentiles A	5.5×10^{-4};2.9×10^{-3}	1.3×10^{-4};9.9×10^{-4}	1.8×10^{-4};7.3×10^{-4}	1.3×10^{-3};3.4×10^{-3}
Median B	1.96×10^{-3}	1.25×10^{-3}	1.94×10^{-3}	4.0×10^{-3}
Percentiles B	6.7×10^{-4};6.7×10^{-3}	5.4×10^{-4};3.6×10^{-3}	9.1×10^{-4};5.9×10^{-3}	2.0×10^{-3};8.6×10^{-3}
Median BC	5.8×10^{-4}	3.6×10^{-4}	1.02×10^{-3}	2.34×10^{-3}
Percentiles BC	2.4×10^{-4};2.6×10^{-3}	1.2×10^{-4};9.0×10^{-4}	4.2×10^{-4};3.1×10^{-3}	9.4×10^{-4};5.0×10^{-3}
Median AB	3.1×10^{-3}	1.9×10^{-4}	6.0×10^{-4}	5.8×10^{-3}
Percentiles AB	1.7×10^{-3};6.3×10^{-3}	6.1×10^{-5};4.7×10^{-4}	2.5×10^{-4};3.1×10^{-3}	3.0×10^{-3};9.7×10^{-3}
Median ABC	4.4×10^{-3}	1.9×10^{-4}	9.0×10^{-4}	9.5×10^{-3}
Percentiles ABC	1.9×10^{-3};8.8×10^{-2}	$6.1E \times 10^{-5}$;4.4×10^{-4}	4.3×10^{-4};2.2×10^{-3}	4.3×10^{-3};1.8×10^{-2}
Median temperature (°C)	2.7	-3.4	5.1	12.4
Percentiles temperature	0.9;4.2	-6;-1.2	2.5;8.1	10.1;15.1
Median wind speed ($\mathrm{ms^{-1}}$)	6.8	6.8	6.5	5.3
percentiles wind speed	4.9;8.3	4.8;9	4.8;8.4	3.8;7.3
Percentage in cloud (%)	39	43	6	16

(b) shows, that while both A and TAP concentrations rose, the increase was not simultaneous. However $\mathrm{NO_x}$ and $\mathrm{SO_2}$ levels increased concurrently with A particles. Therefore, air, polluted with these trace gasses also carried A particles, suggesting, that A particles arriving at the station were anthropogenic in origin, rather than biological.

S3.3 May 7 - 25, 2023: Peak B and BC concentrations

Three distinct peaks in B and BC concentrations occurred in May 2023, around the 10th, 16th and 24th. Back trajectories show that during the latter two peaks, air masses remained close to the surface over the Gulf of Bothnia for three days before arriving at the station (Fig. S7 (b) and (c)). A likely cause is a coastal inversion, which trapped pollutants and led to a sharp rise in B and BC particle concentrations. Figure S7 (d) displays B and BC particle size distributions, revealing a simultaneous increase in both types. B particles dominated below 1 $\mu\mathrm{m}$, while BC particles were mostly > 2 $\mu\mathrm{m}$. Since fluorescence intensity depends on particle size (Hill et al., 2001), it is plausible that both types share the same origin, but only larger particles exceeded the fluorescence threshold in FL3, classifying them as BC rather than B particles. During the same period, eBC mass concentration increased similarly. The strong overall correlation of B and BC concentration and eBC throughout the whole measurement period suggests that these particles largely consist of black carbon. Even during the first peak (Fig. S7(a)), when only a small fraction of air masses had passed over the Gulf of Bothnia, eBC concentrations still increased simultaneously.

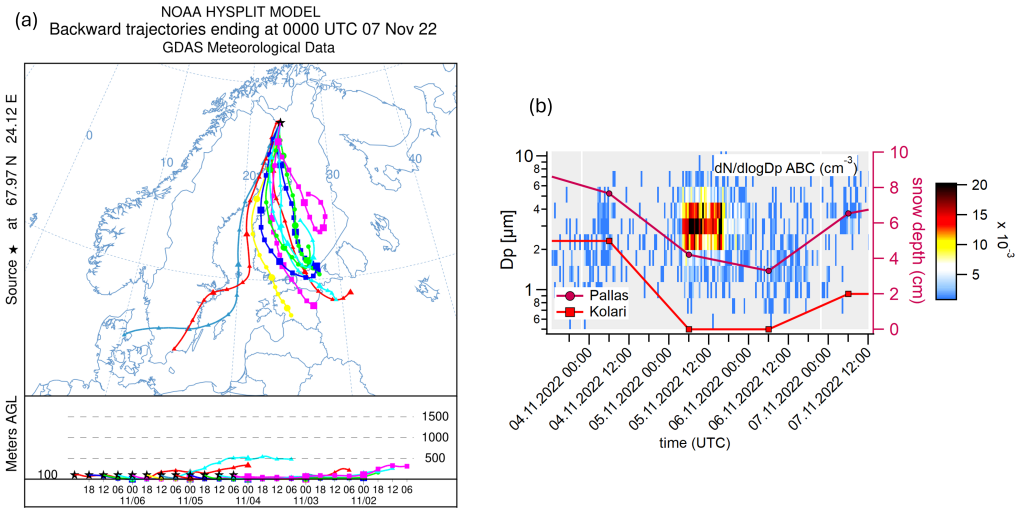

Figure S5. Case study of the prominent ABC concentration peak (labeled (1) in Fig. S2) during temporary snowmelt. (a) HYSPLIT back trajectories from 04.11. 00:00 - 06.11. 24:00. The direction of arriving air masses only changed marginally during the 3 days. (b) Size distribution of ABC particles and snow depth in Pallas (Kenttärova) and Kolari (Kattilamaa) approximately 70 km south of Pallas. In Kolari, snow melted completely and air masses passed that region from the south, probably bringing bioaerosols from the snow free biosphere with them. Grey areas in (b) correspond to a concentration < 0.001 cm^{-3}.

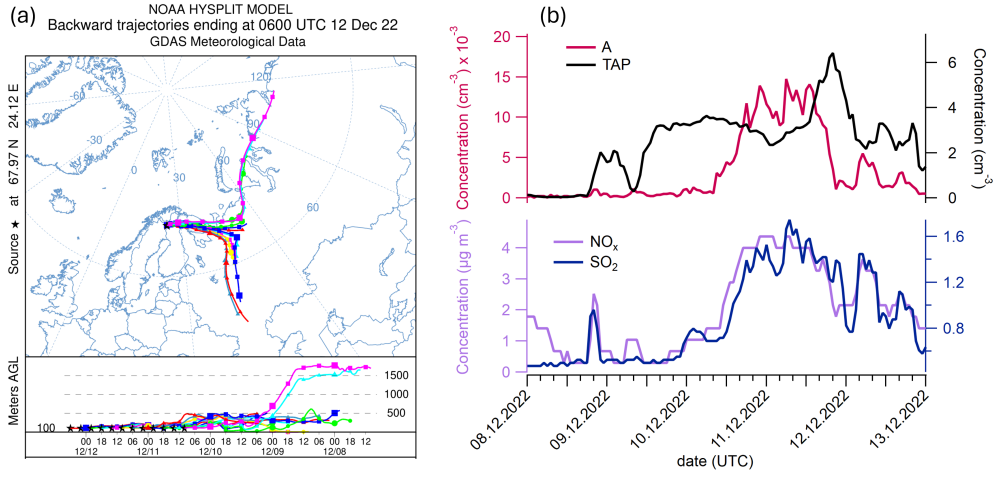

Figure S6. Case study of December 11, 2023 and days around. (a) HYSPLIT back trajectories show that arriving air masses passed over a major industry zone of Russia. (b) Concentrations of A particles, TAPs, $\mathrm{NO_x}$ and $\mathrm{SO_2}$. The latter two increase roughly at the same time as A particles, whereas the TAP concentration behaves differently.

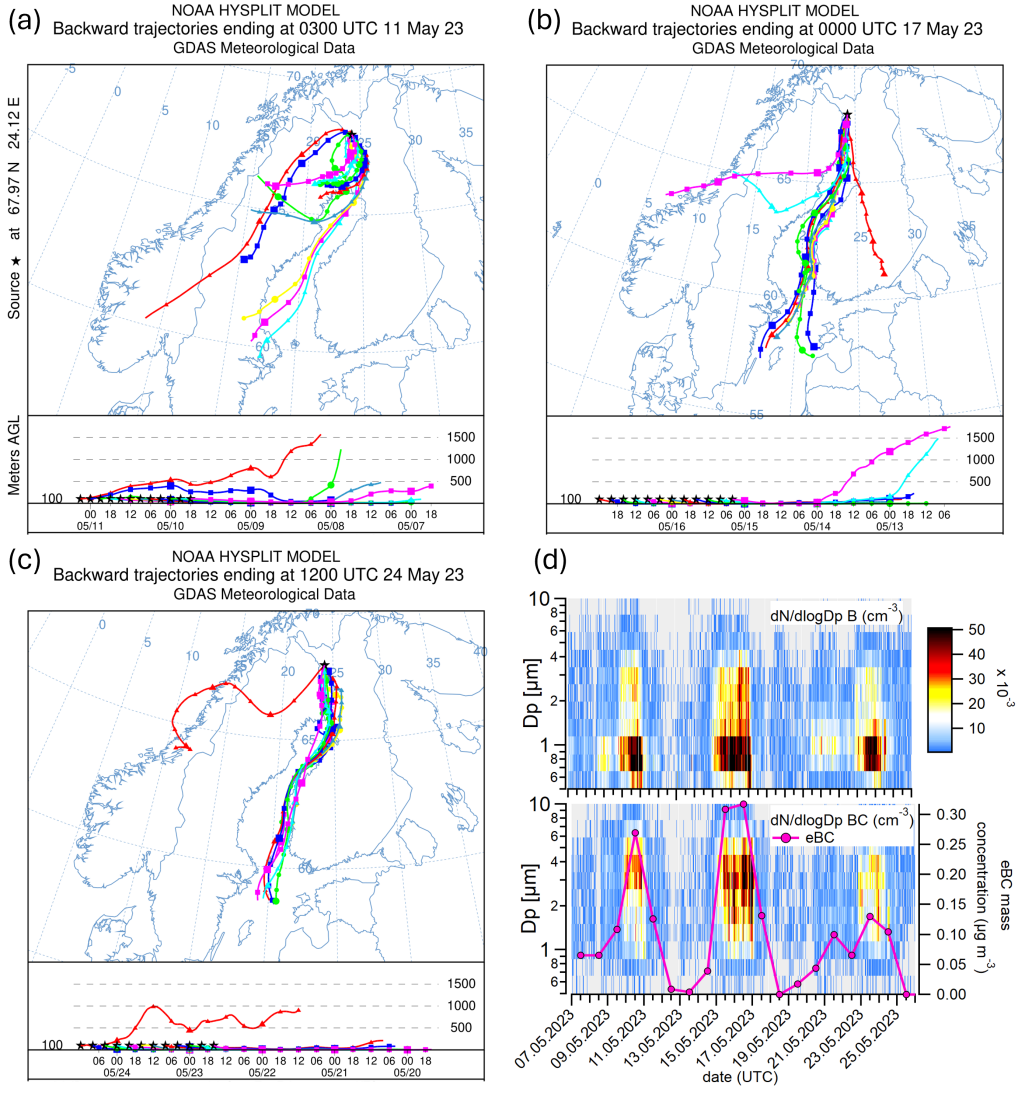

Figure S7. Case study of three prominent peaks of B and BC particle concentrations during may 2023. HYSPLIT back trajectories of (a) May 9, 6 pm - May 11, 3 am, (b) May 15, 4 am - May 17, 12 midnight, (c) May 22, 3 am - May 24, 12 noon (d): size distribution of B particles (top) and BC particles (bottom) as well as mass concentration of eBC (bottom). Grey areas indicate a concentration of less then 0.001 cm^{-3}. The three time periods of the plotted trajectories align with the three concentration peaks in (d).

S3.4 02.08.2023: PEAK AB and ABC concentration

On the August 2, 2023 the maximum concentration of both AB and ABC particle concentrations were recorded. 72 h HYSPLIT back trajectories for this day show, that air masses arriving 100 m above ground came from the south and stayed close to the ground and therefore passed over heavily wooded terrain (Fig. S8 (a)). A comparison to air masses arriving 500 m above

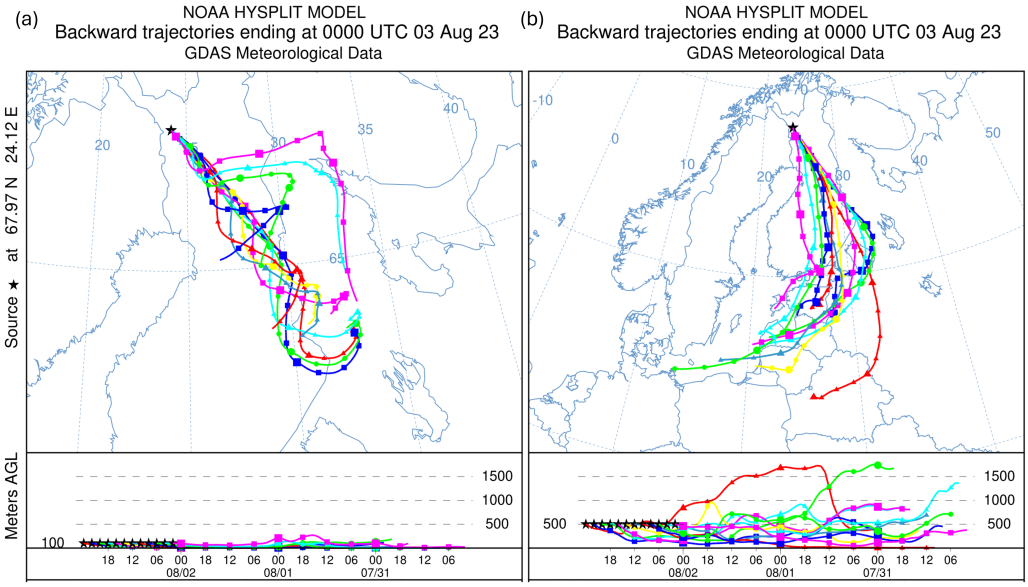

Figure S8. HYSPLIT back trajectories for August 2, 2023. (a) Air masses arriving 100 m above ground level. (b) Air masses arriving 500 m above ground level. In both cases air masses pass over the Finish boreal forest close to the ground.

ground level show that they have covered a longer distance but most of them reached lower altitudes prior arrival above the station, indicating that at 500 m altitude, still regional emitted biological particles are the prominent source of AB and ABC particles.

S4 Inside cloud and precipitation

Throughout the measurement period, the station was inside clouds 27 % of the time (autumn: 39 %, winter: 43 %, spring: 6 %, summer: 16 %). Cloud immersion reduced TAP and HFAP concentrations due to cloud and rain scavenging (Flossmann and Wobrock, 2010; Sellegri et al., 2003). However, TAP (and NON-HFAP) concentrations declined stronger, leading to a strong increase in fluorescent fraction for most in-cloud cases. Median values of concentrations, fractions and the change of both from out-of-cloud to in-cloud times are listed in Tab. S2 for the snow free period. During in-cloud periods, TAP concentrations dropped by 69 %, HFAPs by 51 %, and ABC by 34 %, resulting in a 128 % increase in HFAP fraction and a 232 % rise for ABC fraction. Two exemplary periods with several transitions from cloud free to cloud covered conditions are depicted in Fig. S9: For most cloud events, HFAP concentrations rapidly decreased (logarithmic scale), while the fraction simultaneously increased. This effect was almost instantly reversed after the stations was out-of-cloud again. A similar effect was observed by Crawford et al. (2016) at the high altitude Jungfraujoch station. The authors suggested that non-fluorescent aerosols are more effectively removed through cloud condensation nuclei (CCN) activation and subsequent precipitation in mixed-phase clouds,

Table S2. Median concentrations (conc.) and fractions (fr.) of TAPs and HFAPs for out-of-cloud and in-cloud times during the snow free period and the decrease in concentration and increase in fraction from out-of-cloud to in-cloud times.

	out of cloud		in cloud		change	
Type	median conc. (cm^{-3})	median fr.	median conc. (cm^{-3})	median fr.	decrease of conc. (%)	increase of fr. (%)
TAP	0.7126		0.2219		69	
HFAP	0.0251	0.0279	0.0122	0.0636	51	128
A	0.0020	0.0025	0.0008	0.0039	59	56
B	0.0038	0.0054	0.0022	0.0104	43	94
AB	0.0049	0.0057	0.0027	0.0139	46	145
BC	0.0020	0.0028	0.0009	0.0041	56	45
ABC	0.0074	0.0077	0.0049	0.0257	34	232

whereas fluorescent aerosols remain in the interstitial phase. Recent research supports this, indicating that bioaerosols are poor CCNs under in situ conditions, which may hinder their potential to act as ice nuclei (Šantl Temkiv et al., 2024).

Figure S9 also displays rain intensity for the selected periods. As discussed in Sect. 4 of the main manuscript, we generally did not observe an increase in HFAP concentrations during or after rainfall. Notably, during most rain events shown, the station was also immersed in cloud, suggesting that cloud and rain scavenging suppressed aerosol concentrations. This likely outweighs the rain-related enhancements in bioaerosols reported by previous studies (Rathnayake et al., 2017; Yue et al., 2016; Gosselin et al., 2016; Heo et al., 2014; Schumacher et al., 2013; Huffman et al., 2013; Prenni et al., 2013; Allitt, 2000; Hirst and Stedman, 1963; Gregory and Hirst, 1957). To provide context for the examples in Fig. S9, rain occurred during approximately 23 % of the snow free measurement period. Rain events varied greatly in duration and intensity, ranging from brief light showers to multi-day episodes of sustained precipitation. The two case studies shown represent different types of rainfall patterns commonly encountered during the campaign.

S5 ABC particle thresholds

For the second part of the campaign (April to September 2023) each ABC particle was analyzed individually. From all detected particles, only those exceeding the 9-sigma threshold in all three fluorescence channels (with newly measured thresholds every six hours) were classified as ABC particles. For these particles, daily mean FL1 intensity distributions were calculated by binning intensity values into 24 logarithmically equidistant channels. Figure S10 (a) presents a surface plot of the intensity distributions: On the top the absolute ABC particle count in every intensity channel is described by the color scale. On the bottom the relative contribution of particle counts is plotted. This revealed 3 distinct intensity maxima, with minima between them marked as pink dashed lines in S10 (a) (top). These minima were used to define new FL1 thresholds, leading to the classification of three particle subtypes: ABC_1, ABC_2, and ABC_3. ABC_1 particles have the lowest FL1 intensity with a maximum of 7.9×10^7. ABC_2 posses medium FL1 intensity that ranges between 7.9×10^7 and 7.0×10^8. ABC_3 show the highest intensity with a threshold of 1.0×10^9. Daily mean concentrations of these new particle types are shown in Fig.

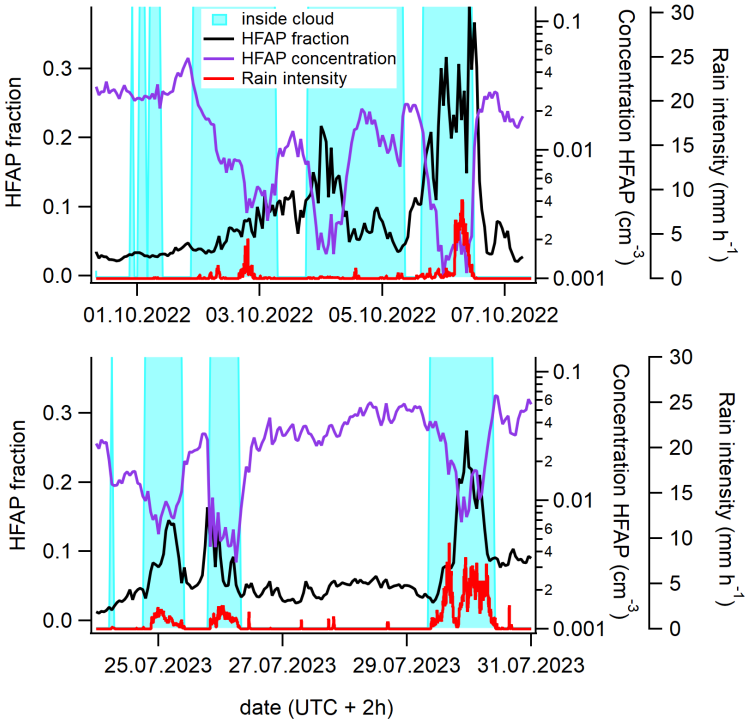

Figure S9. Two examples of the change of concentration and fraction of HFAPs from out-of-cloud to in-cloud transition and rain intensity.

S10 (b). All three types show different temporal behavior. ABC_2 concentrations remain near zero until the end of June and increase until early August. ABC_3 concentrations peak at the end of June, remain low afterwards and are close to zero from mid July onward. This low concentration after mid July probably comes from the upper tail of ABC_2 intensity distribution, as the fluorescence intensity maximum shifts away from the highest intensity channel (see S10 (a) bottom). Section 3.6 of the main text demonstrates that ABC_3 particles correlate with pollen grains. Interestingly, ABC_1 and ABC_2 did not exhibit stronger correlations with fungal spore counts or INP concentrations when analyzed separately, compared to their combined sum.

S6 Microscopy picture of fungal spores and trilete spores

Figure S12 shows a microscopic picture of a Burkard slide from August 28, at 06:00 (UTC+3). Black Arrows point to particles that were reliable identified as fungal spores. Pink arrows point to particles that were believed to be fungal spores, but the identification was slightly uncertain. The yellow arrow points to a cluster of fungal spores and other particles. Please mind, that the picture only represents one focal plane, whereas during the identification, the focus was changed in order to identify a

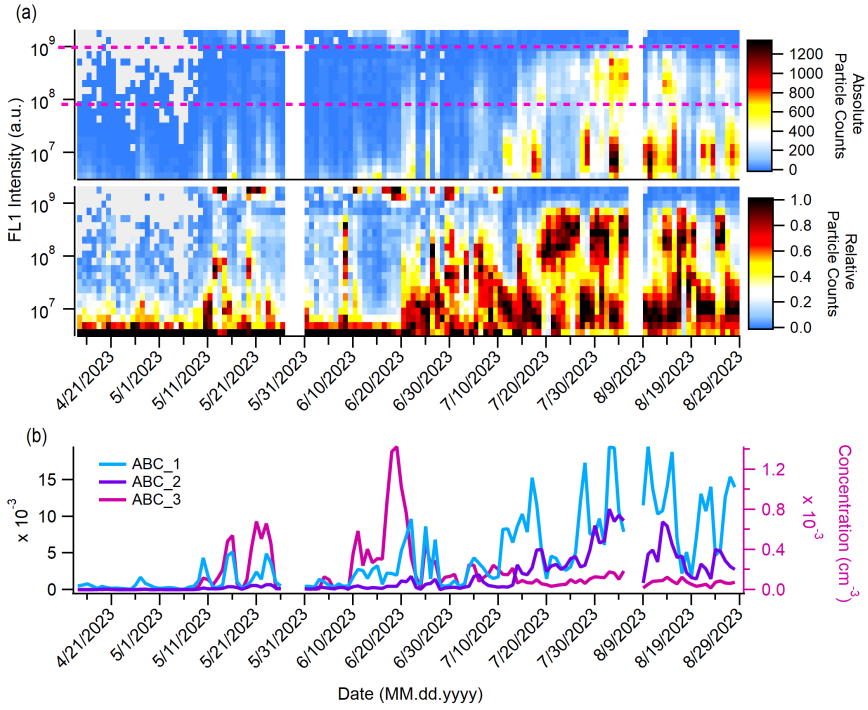

Figure S10. FL1 Intensity distribution for the definition of new fluorescence thresholds of ABC particles. (a) top: Evolution of daily mean particle counts in logarithmic equidistant intensity channels. Pink dashed lines indicate the upper threshold for ABC_1 and the lower threshold for ABC_2 at 7.9×10^7 and the lower threshold for ABC_3 at 1.0×10^9. (a) bottom: Same as top, but normalized to a total particle count of 1 for each day. (b): Daily mean concentrations for ABC_1, ABC_2 and ABC_3 calculated from the new thresholds.

particle as a fungal spore. Figure S12 shows a microscopic picture of two trilete spores and some fungal spores from August 19, at 1 pm (UTC+3).

S7 INP measurements

Figure S13 shows Ice nulceation particle (INP) concentrations active between -6 °C and -23 °C, measured using filters and analyzed with INSEKT. Figure S14 presents INP concentrations active between -23 °C and -31 °C, obtained with PINE and averaged to 1 h intervals. The PINE instrument can either measure INP concentrations at a fixed temperature over an extended period, or it scans a temperature range to record INP activity across multiple temperatures within a shorter time frame. As a result, some periods contain data for all temperatures, while others report only one. Table S3 summarizes Pearson correlation coefficients and corresponding p-values for the relation between WIBS particle concentrations and INP concentrations including only statistically significant correlations ($p < 0.05$).

	INPs active above	-9 °C	-10 °C	-11 °C	-12 °C	-13 °C	-14 °C	-15 °C	-16 °C	-17 °C	-18 °C	-23 °C	-25 °C)	-27 °C	-29 °C	-31 °C
	resolution	1 week	1 week	1 week	1 week	1 week	1 week	1 week	1 week	1 week	1 week	1 hour	1 hour	1 hour	1 hour	1 hour
TAP	Pearson r		0.58									0.21	0.28	0.13	0.26	0.31
	p-value		*									**	**	*	**	**
HFAP	Pearson r	0.64	0.60	0.81	0.80	0.84	0.82	0.81	0.56	0.52	0.46	0.46	0.42	0.47	0.32	0.39
	p-value	*	*	**	**	**	**	**	*	*	*	**	**	**	**	**
FL1	Pearson r	0.59	0.47	0.81	0.85	0.90	0.89	0.78	0.56	0.54		0.45	0.38	0.44	0.35	0.41
	p-value	*	*	**	**	**	**	**	*	*		**	**	**	**	**
FL2	Pearson r	0.63	0.58	0.81	0.80	0.84	0.82	0.82	0.58	0.54	0.48	0.45	0.37	0.45	0.30	0.37
	p-value	*	*	**	**	**	**	**	*	*	*	**	**	**	**	**
FL3	Pearson r	0.61	0.53	0.84	0.84	0.88	0.85	0.84	0.61	0.59	0.50	0.45	0.27	0.42	0.29	0.35
	p-value	*	*	**	**	**	**	**	*	*	*	**	**	**	**	**
A	Pearson r	0.59	0.57	0.64	0.63	0.67	0.70	0.50				0.45	0.50	0.47	0.43	0.49
	p-value	*	*	*	*	*	**	*				**	**	**	**	**
B	Pearson r		0.56									0.39	0.41	0.37	0.23	0.32
	p-value		*									**	**	**	**	**
AB	Pearson r	0.56	0.45	0.74	0.79	0.85	0.86	0.71	0.49	0.48		0.42	0.28	0.44	0.35	0.40
	p-value	*	*	**	**	**	**	**	*	*		**	**	**	**	**
BC	Pearson r		0.51					0.53				0.43	0.35	0.39	0.27	0.34
	p-value		*					*				**	**	**	**	**
ABC	Pearson r	0.57		0.83	0.87	0.92	0.89	0.81	0.61	0.60		0.43	0.22	0.38	0.29	0.34
	p-value	*		**	**	**	**	**	*	*		**	**	**	**	**
AB+ABC	Pearson r	0.60	0.48	0.82	0.86	0.91	0.89	0.79	0.58	0.57		0.43	0.24	0.41	0.32	0.37
	p-value	*	*	**	**	**	**	**	*	*		**	**	**	**	**

Table S3. Pearson correlation analysis. *: p<0.05, ** p<0.0001

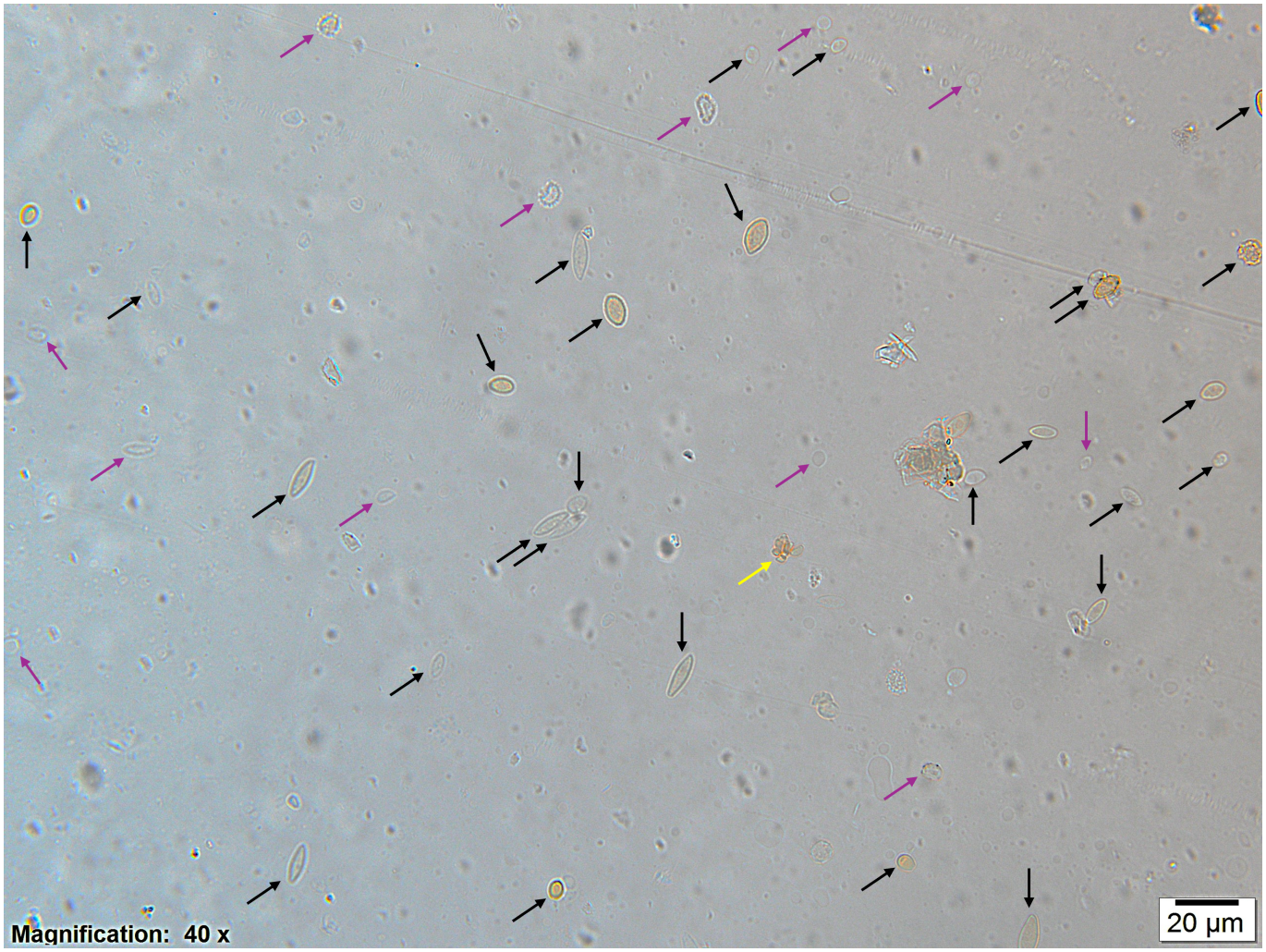

Figure S11. An example of fungal spore counts from August 28, 2023, 6 am (UTC+3). Black arrows point to reliable identified fungal spores, pink arrows point to particles that are probably fungal spores and the yellow arrow points to a cluster of fungal spores and other particles.

S8 Impactor measurements

In parallel with INP and eDNA filter sampling, a Sioutas Personal Cascade Impactor was used (described in the main text, Section 2). Fluorescent particle concentrations were determined by analyzing stages A and B: (Da > 2.5 µm and 1.0 < Da < 2.5 µm, respectively). Fluorescent particles were examined using a fluorescence microscope. The impacted area was estimated by measuring its length with a slide gauge and its width at three different positions using microscope software. For each stage, three images of fluorescent particles (λ_{ex}=465–495 nm, λ_{ex}=515–555 nm) were taken at approximately the middle, one-quarter, and three-quarters of the impaction area length using a 10x magnification. Fluorescent particles were counted in ImageJ after setting an automatic threshold via the triangle method. The image area was then compared to the total impaction

Figure S12. An example of trilete spore counts from August 19, 2023, 1 pm (UTC+3). Black arrows point to reliable identified trilete spores. Some fungal spores are also visible but not marked.

area. A mean value and standard deviation were calculated from three measurements per impaction foil. The total number of fluorescent particles >1.0 µm (aerodynamic diameter) was determined by summing particle counts from stages A and B. Concentrations were then calculated by dividing by the air volume passing through the impactor. Concentrations of fluorescent particles were probably underestimated with this method due to bouncing of particles and subsequent impaction on lower stages that were not examined.

The resulting concentration, as well as the concentration of INPs active at -14.5 °C is plotted in Fig. S15. Both concentrations stay relatively constant for 6 measurements (5 for the impactor) before dropping by approximately one order of magnitude

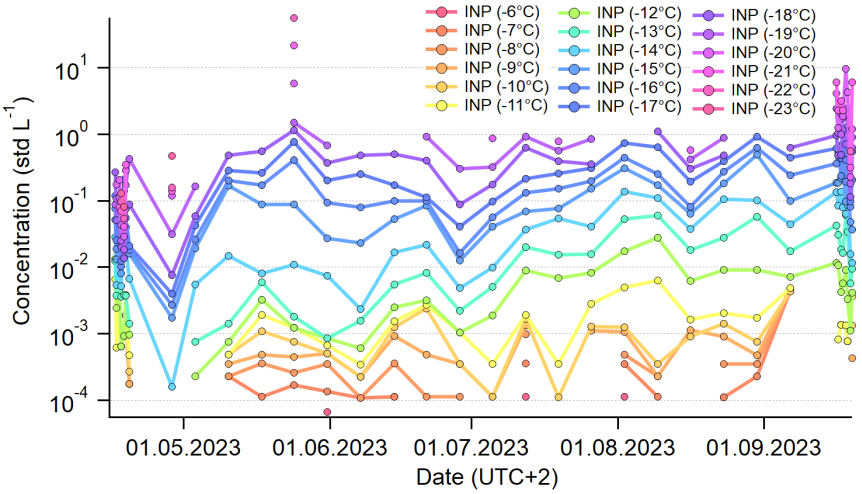

Figure S13. INP concentrations measured with INSEKT.

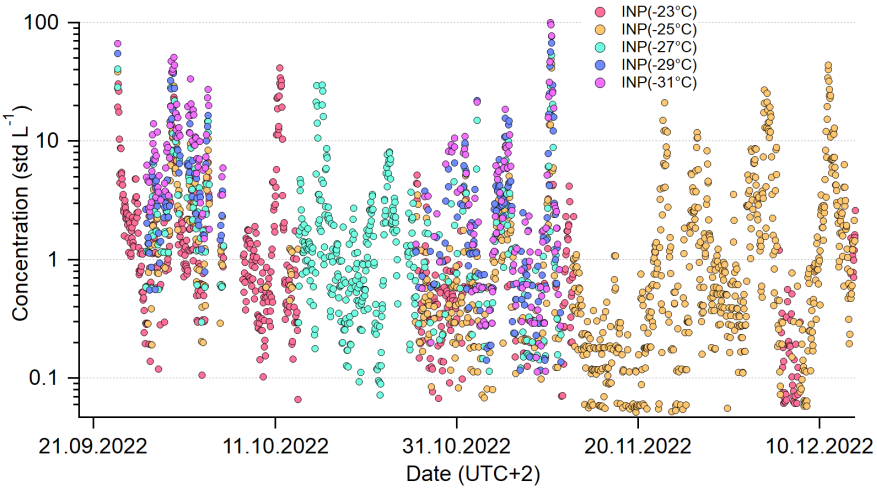

Figure S14. Low temperature INP concentrations measured with PINE.

during the final two measurements, coinciding which a snow storm. Most of the fluorescent particles examined in detail were identified as fungal spores (see main text sect. 3.6, Fig. 8).

S9 AB concentrations in relation to meteorology

160 The relationship of median AB concentrations for each season is shown in Fig. S16 and reveals strong similarities to ABC concentrations.

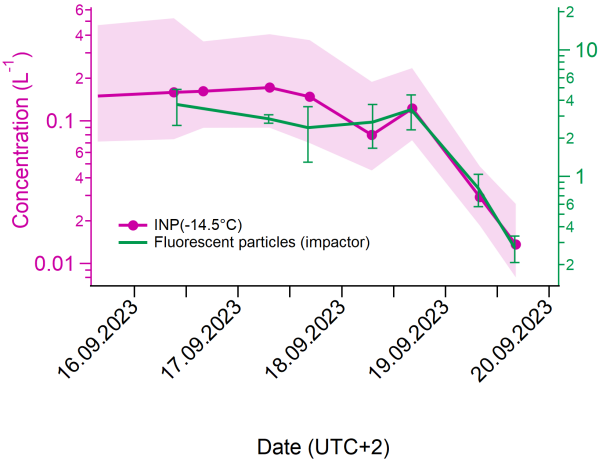

Figure S15. INP concentration at -14.5 °C and concentration of fluorescent particles > 1 µm (aerodynamic diameter) impacted on stage A and B on the cascade impactor.

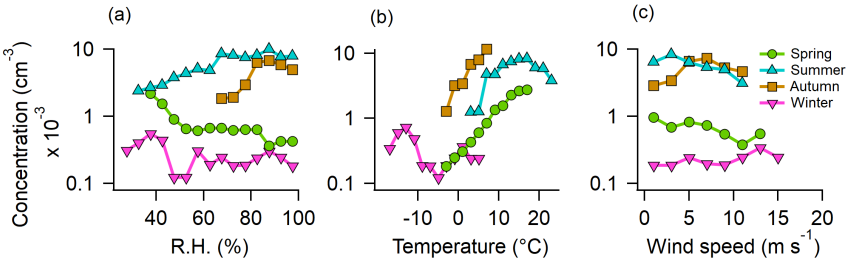

Figure S16. The median concentration of AB particles dependent on meteorological parameters for each season. Depicted are median concentration values for 1 h mean values. (a) R.H., (b) ambient Temperature, (c) wind speed.

References

Abdel Hameed, A., Khoder, M., Yuosra, S., Osman, A., and Ghanem, S.: Diurnal distribution of airborne bacteria and fungi in the atmosphere of Helwan area, Egypt, Sci Total Environ, 407, 6217–6222, https://doi.org/10.1016/j.scitotenv.2009.08.028, 2009.

Allitt, U.: Airborne fungal spores and the thunderstorm of 24 June 1994, Aerobiologia, 16, 397–406, https://doi.org/10.1023/A:1026503500730, 2000.

Bauer, H., Kasper-Giebl, A., Löflund, M., Giebl, H., Hitzenberger, R., Zibuschka, F., and Puxbaum, H.: The contribution of bacteria and fungal spores to the organic carbon content of cloud water, precipitation and aerosols, Atmospheric Research, 64, 109–119, https://doi.org/10.1016/S0169-8095(02)00084-4, 2nd International Conference on Fog and Fog Collection, 2002.

Burrows, S. M., Elbert, W., Lawrence, M. G., and Pöschl, U.: Bacteria in the global atmosphere – Part 1: Review and synthesis of literature data for different ecosystems, Atmospheric Chemistry and Physics, 9, 9263–9280, https://doi.org/10.5194/acp-9-9263-2009, 2009.

Crawford, I., Lloyd, G., Herrmann, E., Hoyle, C. R., Bower, K. N., Connolly, P. J., Flynn, M. J., Kaye, P. H., Choularton, T. W., and Gallagher, M. W.: Observations of fluorescent aerosol–cloud interactions in the free troposphere at the High-Altitude Research Station Jungfraujoch, Atmos Chem Phys, 16, 2273–2284, https://doi.org/10.5194/acp-16-2273-2016, 2016.

Després, V., Huffman, J. A., Burrows, S. M., Hoose, C., Safatov, A., Buryak, G., Fröhlich-Nowoisky, J., Elbert, W., Andreae, M., Pöschl, U., et al.: Primary biological aerosol particles in the atmosphere: a review, Tellus B: Chem Phys Meteorol, 64, 15 598, https://doi.org/10.3402/tellusb.v64i0.15598, 2012.

Flossmann, A. I. and Wobrock, W.: A review of our understanding of the aerosol–cloud interaction from the perspective of a bin resolved cloud scale modelling, Atmos Res, 97, 478–497, https://doi.org/10.1016/j.atmosres.2010.05.008, from the Lab to Models and Global Observations: Hans R. Pruppacher and Cloud Physics, 2010.

Gosselin, M. I., Rathnayake, C. M., Crawford, I., Pöhlker, C., Fröhlich-Nowoisky, J., Schmer, B., Després, V. R., Engling, G., Gallagher, M., Stone, E., Pöschl, U., and Huffman, J. A.: Fluorescent bioaerosol particle, molecular tracer, and fungal spore concentrations during dry and rainy periods in a semi-arid forest, Atmos Chem Phys, 16, 15 165–15 184, https://doi.org/10.5194/acp-16-15165-2016, 2016.

Gratzl, J., Brus, D., Doulgeris, K., Böhmländer, A., Möhler, O., and Grothe, H.: Fluorescent aerosol particles in the Finnish sub-Arctic during the Pallas Cloud Experiment 2022 campaign, Earth Syst Sci Data Discuss, 2025, 1–20, https://doi.org/10.5194/essd-2024-543, 2025.

Gregory, P. H. and Hirst, J. M.: The Summer Air-Spora at Rothamsted in 1952, Microbiology, 17, 135–152, https://doi.org/10.1099/00221287-17-1-135, 1957.

Healy, D., Huffman, J., O'Connor, D. J., Pöhlker, C., Pöschl, U., and Sodeau, J.: Ambient measurements of biological aerosol particles near Killarney, Ireland: a comparison between real-time fluorescence and microscopy techniques, Atmos Chem Phys, 14, 8055–8069, https://doi.org/10.5194/acp-14-8055-2014, 2014.

Heo, K. J., Kim, H. B., and Lee, B. U.: Concentration of environmental fungal and bacterial bioaerosols during the monsoon season, J Aersosol Sci, 77, 31–37, https://doi.org/10.1016/j.jaerosci.2014.07.001, 2014.

Hernandez, M., Perring, A. E., McCabe, K., Kok, G., Granger, G., and Baumgardner, D.: Chamber catalogues of optical and fluorescent signatures distinguish bioaerosol classes, Atmos Meas Tech, 9, 3283–3292, https://doi.org/10.5194/amt-9-3283-2016, 2016.

Hill, S. C., Pinnick, R. G., Niles, S., Fell, N. F., Pan, Y.-L., Bottiger, J., Bronk, B. V., Holler, S., and Chang, R. K.: Fluorescence from airborne microparticles: dependence on size, concentration of fluorophores, and illumination intensity, Appl Opt, 40, 3005–3013, https://doi.org/10.1364/ao.40.003005, 2001.

Hirst, J. M. and Stedman, O. J.: Dry Liberation of Fungus Spores by Raindrops, Microbiology, 33, 335–344, https://doi.org/10.1099/00221287-33-2-335, 1963.

Huffman, J. A., Prenni, A., DeMott, P., Pöhlker, C., Mason, R., Robinson, N., Fröhlich-Nowoisky, J., Tobo, Y., Després, V., Garcia, E., et al.: High concentrations of biological aerosol particles and ice nuclei during and after rain, Atmos Chem Phys, 13, 6151–6164, https://doi.org/10.5194/acp-13-6151-2013, 2013.

Katsivela, E., Chatoutsidou, S. E., Saridaki, A., Raisi, L., Stathopoulou, P., Tsiamis, G., Kunfeng, G., Fetfatzis, P., Romanos, F., Gidarakou, M., Gini, M. I., Granakis, K., Mylonaki, M., Papanikolaou, C., Vratolis, S., Vogel, F., Zografou, O., Möhler, O., Papayannis, A., Eleftheriadis, K., Nenes, A., and Lazaridis, M.: Airborne Microorganisms at Hellenic Atmospheric Aerosol and Climate Change Station in Helmos Mountain (Greece), https://doi.org/10.1021/acsearthspacechem.5c00064, 2025.

Lighthart, B. and Shaffer, B. T.: Airborne Bacteria in the Atmospheric Surface Layer: Temporal Distribution above a Grass Seed Field, Appl Environ Microbiol, 61, 1492–1496, https://doi.org/10.1128/aem.61.4.1492-1496.1995, 1995.

Prenni, A., Tobo, Y., Garcia, E., DeMott, P., Huffman, J., McCluskey, C., Kreidenweis, S., Prenni, J., Pöhlker, C., and Pöschl, U.: The impact of rain on ice nuclei populations at a forested site in Colorado, Geophys Res Lett, 40, 227–231, https://doi.org/10.1029/2012GL053953, 2013.

Rathnayake, C. M., Metwali, N., Jayarathne, T., Kettler, J., Huang, Y., Thorne, P. S., O'Shaughnessy, P. T., and Stone, E. A.: Influence of rain on the abundance of bioaerosols in fine and coarse particles, Atmos Chem Phys, 17, 2459–2475, https://doi.org/10.5194/acp-17-2459-2017, 2017.

Savage, N. J., Krentz, C. E., Könemann, T., Han, T. T., Mainelis, G., Pöhlker, C., and Huffman, J. A.: Systematic characterization and fluorescence threshold strategies for the wideband integrated bioaerosol sensor (WIBS) using size-resolved biological and interfering particles, Atmos Meas Tech, 10, 4279–4302, https://doi.org/10.5194/amt-10-4279-2017, 2017.

Schumacher, C., Pöhlker, C., Aalto, P., Hiltunen, V., Petäjä, T., Kulmala, M., Pöschl, U., and Huffman, J.: Seasonal cycles of fluorescent biological aerosol particles in boreal and semi-arid forests of Finland and Colorado, Atmos Chem Phys, 13, 11 987–12 001, https://doi.org/10.5194/acp-13-11987-2013, 2013.

Sellegri, K., Laj, P., Dupuy, R., Legrand, M., Preunkert, S., and Putaud, J.-P.: Size-dependent scavenging efficiencies of multicomponent atmospheric aerosols in clouds, J Geophys Res: Atmos, 108, https://doi.org/10.1029/2002JD002749, 2003.

Yue, S., Ren, H., Fan, S., Sun, Y., Wang, Z., and Fu, P.: Springtime precipitation effects on the abundance of fluorescent biological aerosol particles and HULIS in Beijing, Sci Rep, 6, 29 618, https://doi.org/10.1038/srep29618, 2016.

Šantl Temkiv, T., Živec, M., Lund, M. B., Benčina, M., Bohn, A. B., Stanič, S., and Močnik, G.: The limited capacity of bioaerosols to serve as cloud-condensation nuclei may restrict their potential to initiate ice formation in mixed-phase clouds, bioRxiv, p. 2024.10.30.621021, https://doi.org/10.1101/2024.10.30.621021, 2024.